

# Self-forming nanocomposite concept for ZnO-based thermoelectrics

Kiryl V. Zakharchuk <sup>a</sup>, Marc Widenmeyer <sup>b</sup>, Denis O. Alikin <sup>a,c</sup>, Wenjie Xie <sup>b</sup>, Sascha Populoh <sup>d,e</sup>,

Sergey M. Mikhalev <sup>f</sup>, Alexander Tselev <sup>a</sup>, Jorge R. Frade <sup>a</sup>, Anke Weidenkaff <sup>b</sup>,

Andrei V. Kovalevsky\* <sup>a</sup>

<sup>a</sup> CICECO – Aveiro Institute of Materials, Department of Materials and Ceramic Engineering, University of Aveiro, 3810-193 Aveiro, Portugal;

<sup>b</sup> Materials Chemistry, Institute for Materials Science, University of Stuttgart, Heisenbergstr. 3, DE-70569 Stuttgart, Germany;

<sup>c</sup> School of Natural Sciences and Mathematics, Ural Federal University, Ekaterinburg, Russian Federation;

<sup>d</sup> Empa, Materials for Energy Conversion, Ueberlandstr. 129, CH-8600 Duebendorf, Switzerland;

<sup>e</sup> ABB Switzerland Ltd., Semiconductors, Fabrikstrasse 3, CH-5600 Lenzburg, Switzerland;

<sup>f</sup> TEMA-NRD, Mechanical Engineering Department, Aveiro Institute of Nanotechnology (AIN), University of Aveiro, 3810-193 Aveiro, Portugal

\* Corresponding author. Present address: Department of Materials and Ceramic Engineering, CICECO, University of Aveiro, 3810-193 Aveiro, Portugal.  
Fax: +351-234-370204; Tel: +351-234-370235; E-mail: akavaleuski@ua.pt

## **Abstract**

Zinc oxide (ZnO) has a very broad and versatile range of applications provided by high abundance, optical and electrical properties, which can be further tuned by donor substitution. Al-doped ZnO is probably the most thoroughly investigated material regarding thermoelectric properties. Fairly reasonable electrical properties of donor-doped zinc oxide are usually combined with a high thermal conductivity limiting potential applications. Here we report a new self-forming nanocomposite concept for ZnO-based thermoelectrics, where a controllable interplay between the presence and exsolution of the nanophases, and modification of the host matrix suppresses the thermal transport while imparting enhanced electrical performance. The thermoelectric performance of the best-obtained composite, described by the dimensionless figure-of-merit  $ZT$ , at 920-1200 K is almost twice of the pure matrix composition and reaches up to 0.11. The proposed approach invokes controlled interactions between composite components as a novel tool for decoupling the electrical and thermal transport parameters and shows clear prospects for an implementation in other thermoelectric oxide systems. The results indicate that the proposed concept may also constitute a promising pathway to achieve a stable electrical performance at high temperatures, which currently represents one of the major challenges towards performing ZnO-based thermoelectrics.

**Keywords:** zinc oxide, thermoelectric performance, electrical properties, thermal conductivity, nanocomposite

## 1. Introduction

Zinc oxide (ZnO) is a widely-used and versatile material, possessing an extraordinary combination of useful electrical, optoelectronic, catalytic and photochemical properties<sup>1,2</sup>. The zinc atom has a relatively high electronegativity with a strong preference to sp<sup>3</sup> hybridization, implying that Zn-O bonds are rather covalent; hence, high carrier mobility could be expected in this oxide<sup>3</sup>. Thus, ZnO-based materials were considered for potential applications in thermoelectric devices capable of performing high-temperature heat-to-electricity conversion<sup>3,4</sup>. Thermoelectric conversion is expected to play an important role in future energy technologies provided by simplicity, reliability, and self-sufficiency to enable mobile or remote applications<sup>5-7</sup>. In general, oxides represent a promising alternative to the “traditional” lead-, antimony-, bismuth-, and tellurium-containing thermoelectric materials due to thermal and chemical stability, high natural abundance, and less toxic composition<sup>7-12</sup>. Still, many oxides are not attractive as thermoelectrics mainly due to inherently low charge carrier mobility; consequently, donor-doped ZnO is appealing for seeking high electrical performance. However, while being promising in terms of electrical properties, the high thermal conductivity of ZnO-based oxides represents a principal limiting factor for increasing the thermoelectric performance. The stability and reproducibility of the electrical properties also remain a significant challenge<sup>13,14</sup>, contributing to the large dispersion of the data reported in the literature.

In technological and engineering perspectives, nanostructuring has been proven to provide new opportunities for varying thermoelectric properties ( $\sigma$ ,  $\alpha$ ,  $\kappa$ ) quasi-independently and thus to improve the thermoelectric efficiency<sup>10,15-17</sup>. Formation of low-dimensional structures results in an increase of the phonon interface scattering, consequently reducing the lattice thermal conductivity and improving the dimensionless figure-of-merit  $ZT$ . Effective phonon scattering may occur at the interfaces, created by nanoparticles, embedded in the matrix of a bulk host material. Such nanostructuring can be obtained either by introducing the

nanoparticles during the processing or by in situ formation of the nanoscale precipitates, induced by specific thermal processing conditions of a metastable host matrix<sup>15</sup>. The morphological improvements in nanocomposites leading to an enhanced thermoelectric performance can be categorized by several parameters including dimension scale reduction (bulk, thin film, nanowire, atomic cluster, quantum dot), grain refinement, and reduction of the size of the second phase<sup>10</sup>. Zinc oxide exhibits probably the richest family of nanostructures among all materials<sup>18,19</sup>. Although direct implementation of those nanostructures for efficient thermoelectric energy conversion in thin films is probably possible, it is not viable today due to high associated costs and the complexity of such processing for mass production. A more viable solution implies the fast consolidation of nanostructures to produce nanograin ceramics. Since 2010 this concept emerged as a promising direction in research for well-performing ZnO-based thermoelectrics<sup>20–22</sup>. As an example, an ultra-low thermal conductivity of  $\sim 2.8 \text{ W}\times\text{m}^{-1}\times\text{K}^{-1}$  at room temperature and  $\sim 1.8 \text{ W}\times\text{m}^{-1}\times\text{K}^{-1}$  at 1000 K was achieved in Al-doped ZnO nanocomposites, prepared through consolidation of the nanocrystals<sup>21</sup>. Application of spark plasma sintering (SPS) for sintering of the nanoprecursors allows to avoid significant grain growth and maintain efficient phonon scattering at the grain boundaries<sup>22–25</sup>.

This work demonstrates a new nanocomposite concept for ZnO-based materials, based on both intentional incorporation of the external nanoparticles and in situ formation of the new nanophase, provided by controlled chemical interactions between the components. Aluminum-doped zinc oxide was selected as a model system, owing to relatively well-known interrelations between the phase composition and thermoelectric properties in these materials. A conventional solid-state processing route was involved to emphasize the role of interactions and phase transformations induced by external nanoparticles, while minimizing the effects provided by the differences in the matrix microstructure.

## 2. Experimental

To gain a better understanding of the relevant effects provided by the nanocomposite structure, a series of  $\text{Zn}_{0.993}\text{Al}_{0.007}\text{O-ZrO}_2$  composites based on different  $\text{ZrO}_2$  precursors and several reference compositions were prepared. For the preparation of the nanocomposite series further denoted as ZN (zirconia nano), one used  $\text{ZrO}_2$  nanopowder provided by Sigma-Aldrich with a particles size below 100 nm. The series denoted as TZ (Tosoh zirconia) were prepared based on Tosoh grade TZ-0 zirconia with a particle size of 25-50 nm. The matrix  $\text{Zn}_{0.993}\text{Al}_{0.007}\text{O}$  composition, as well as the reference  $\text{Zn}_{0.993}\text{Zr}_{0.007}\text{O}$  and  $\text{Zn}_{0.994}\text{Al}_{0.003}\text{Zr}_{0.003}\text{O}$  samples, were pre-synthesized by mixing the corresponding amounts of ZnO (Alfa-Aesar, 99.99%),  $\text{Al}_2\text{O}_3$  (Sigma-Aldrich, 99.7%), and Tosoh grade  $\text{ZrO}_2$  TZ-0 precursors. Multiple annealing steps at 1173-1373 K for 5-15 h, with intermediate regrindings were conducted. After subsequent ball-milling with ethanol, drying, and uniaxial compacting, the corresponding ceramics with the density of 87-96% from theoretical was sintered at 1773 K for 5 h in air.

The nanocomposite formulations contained 5, 10, and 20% wt. of  $\text{ZrO}_2$  and are denoted as ZN-5, ZN-10, and ZN-20 in the case of Sigma-Aldrich  $\text{ZrO}_2$  nanopowder, and TZ-5, TZ-10, and TZ-20 when using Tosoh grade zirconia as a nanophase precursor. It should be noticed that, due to similar theoretical densities of ZnO and  $\text{ZrO}_2$ , the zirconia weight content is nearly equal to its volume fraction (e.g., 20% wt. correspond to 19.5% vol.). To improve homogenization, the pre-synthesized  $\text{Zn}_{0.993}\text{Al}_{0.007}\text{O}$  matrix powder was dispersed in alcohol and subjected to ultrasonication, with simultaneous gradual addition of corresponding  $\text{ZrO}_2$  powder. The final mixture was dried by delicate heating under ultrasound; disk-shaped samples were isostatically compacted and sintered at 1773 K for 5 h in air. The densities of sintered nanocomposite samples were within 94-99% of the theoretical density, calculated based on actual volume fractions of the phases and their densities (5.67  $\text{g/cm}^3$  for ZnO-based phase and 5.836  $\text{g/cm}^3$  for monoclinic zirconia<sup>26</sup>).

The sintered ceramic samples were ground to produce fine powders for X-Ray diffraction (XRD) analysis and differential scanning calorimetry (DSC). Both polished and thermally-etched, and freshly-fractured ceramics were characterized by scanning electron microscopy combined with energy dispersive spectroscopy (SEM/EDS). Extra-fine polishing was performed for the samples assessed by scanning thermal microscopy (SThM) and electrostatic force microscopy (EFM). Freshly-cut ceramic rectangular bars were used for the total conductivity and Seebeck coefficient measurements. For the thermal diffusivity studies, ~1.00 mm thick disc-shaped ceramic samples were prepared.

Room-temperature XRD patterns were obtained using a Rigaku D/Max-B diffractometer (Cu K $\alpha$ ) and scanning in the range  $2\theta=10^\circ$ - $80^\circ$ , with a step of  $0.02^\circ$  and an exposition time of 3 s. The microstructural studies were performed by SEM (Hitachi SU-70 instrument) and EDS (Bruker Quantax 400 detector) analysis of the fractured and polished ceramics.

Scanning probe microscopy (SPM) modes (EFM and SThM) were done using a commercial scanning probe microscope Ntegra Aura (NT-MDT, Russia). A SThM controller was used to pass 700  $\mu$ A current through the SThM tip to heat up to 433 K. Balancing of the current by a Wheatstone bridge allowed to visualize the thermal conductivity distribution across the sample. The commercial NT-MDT SThM\_P tips with the curvature less than 100 nm and a spring constant of 0.45 N/m were used. EFM was realized using the internal electronics of the microscope with Budget Sensors ElectriTap300-G tips with curvature less than 25 nm, a resonance frequency of about 300 kHz, and 20 N/m force constant. During conventional two-pass EFM a bias of 2 V DC was applied to the SPM at the second pass at a lift distance of 50 nm.

The electrical properties (total conductivity ( $\sigma$ ) and Seebeck coefficient ( $\alpha$ )) were measured simultaneously in flowing air on stepwise cooling from 1173 K to 573 K, followed by up to 0.5 hours thermal equilibration at each temperature, as described in <sup>27</sup>, or isothermally at 973 and 1173 K. As a rule, the reproducibility error did not exceed 5-9%, as follows from

representative examples of the reproducibility measurements shown in Fig. S1 of the Supplementary Information. In the case of ZnO-based materials, good ohmic contacts for performing electrical measurements represent a certain problem <sup>28</sup>, especially at low temperatures. Therefore, the electrical conductivity data was extrapolated down to 380 K, in order to obtain estimates for the lattice thermal conductivity, as described below. Thermal diffusivity ( $D$ ) and specific heat capacity ( $C_p$ ) studies were performed in air on stepwise cooling from 1173 K to 373 K with a similar thermal equilibration procedure as for the electrical measurements, using a Netzsch LFA 457 Microflash and a Netzsch DSC 404F1, correspondingly. The thermal conductivity ( $\kappa$ ) was calculated as  $\kappa = D\rho c_p$ , where  $\rho$  is the sample density, calculated from the geometrical dimensions and weight of the disk-shaped sample. The lattice thermal conductivity ( $\kappa_{ph}$ ) was calculated from the Wiedemann-Franz' law as:

$$\kappa_{ph} = \kappa - \sigma L T \quad (1)$$

where  $L$  ( $2.45 \cdot 10^{-8} \text{ W} \times \Omega \times \text{K}^{-2}$ ) is the Sommerfeld value of the Lorenz number. In order to account for porosity effects, the experimental data on electrical and thermal conductivities were normalised to 100% density using the Maxwell correction for homogeneously-distributed spherical pores <sup>11,29</sup>.

### 3. Results and discussion

The X-ray diffraction profiles of reference compositions and representative composite materials are shown in Fig. 1.

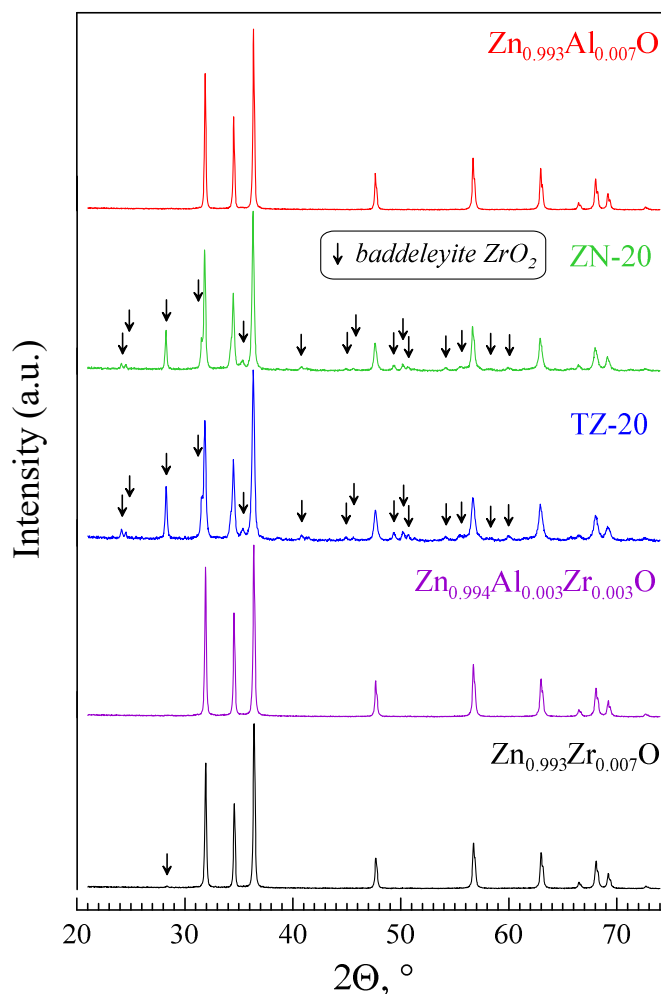


Fig. 1. Room-temperature powder XRD patterns of the representative samples.

All reflections corresponding to the ZnO-based phase can be indexed to a hexagonal wurtzite structure, as expected for the selected doping approach and the processing conditions. The variation in the unit cell volume of the ZnO-based phases ( $47.62\text{-}47.67 \text{ \AA}^3$ ), estimated by the profile matching method in Fullprof software<sup>30</sup>, is close to the experimental error and do not yield any conclusive guidelines on structural effects exerted by doping and/or interaction

between composite phases. This limitation is presumably imposed by relatively low content and solubility of the dopants, along with exsolution and co-doping effects in composites, as discussed below. Monoclinic baddeleyite  $\text{ZrO}_2$  is detected as unique zirconia phase in all composite samples, in accordance with the phase diagrams (<sup>31</sup> and references therein). Minor reflections of a  $\text{ZrO}_2$  impurity phase are also identified for the reference composition  $\text{Zn}_{0.993}\text{Zr}_{0.007}\text{O}$  (Fig. 1), indicating a very limited solubility of zirconium in the zinc oxide lattice, based on the significant size and charge mismatch. Matrix  $\text{Zn}_{0.993}\text{Al}_{0.007}\text{O}$  and reference  $\text{Zn}_{0.994}\text{Al}_{0.003}\text{Zr}_{0.003}\text{O}$  samples are apparently single-phase from XRD studies, while detailed SEM/EDS inspection of corresponding fractured ceramics indicated the presence of vestigial amounts of  $\text{ZnAl}_2\text{O}_4$  and  $\text{ZrO}_2$  impurities (not shown). Yet, a large discrepancy on the solubility limits of aluminium in  $\text{ZnO}$  exists within the available literature data <sup>3,4,21,32-36</sup>, mostly due to associated difficulties in controlling the solubility of a small dopant content, which is very sensitive to the ceramics processing conditions and the thermal/chemical prehistory of the sample.

The microstructural features and effects caused by the grain boundaries are believed to contribute significantly to both heat and charge transport processes in  $\text{ZnO}$ -based materials, especially in nanostructured ceramics <sup>37</sup>. SEM observations at relatively low resolution reveal similar morphology and grain size of the  $\text{ZnO}$ -based phase for all prepared materials, including the reference samples and composites; typical micrographs for the composites are presented in Fig. 2 (A,B). These results, however, suggest that the applied preparation conditions are still not optimal for processing of such nanocomposites. In particular, the SEM micrographs of the  $\text{ZrO}_2$  precursor powders shown in Fig. 2 (C,D) confirm the nanodimensions of the particles, with somewhat higher agglomeration for the powder from Sigma-Aldrich. In sintered composite ceramics the agglomeration of primary  $\text{ZrO}_2$  crystallites into secondary particle assemblies occurs together with the formation of the desired nanocomposite structure, where initial  $\text{ZrO}_2$

particles almost retain their initial size and show a fairly uniform spatial distribution. Fig. 2 (A,B) micrographs feature those distinct microstructural regions.

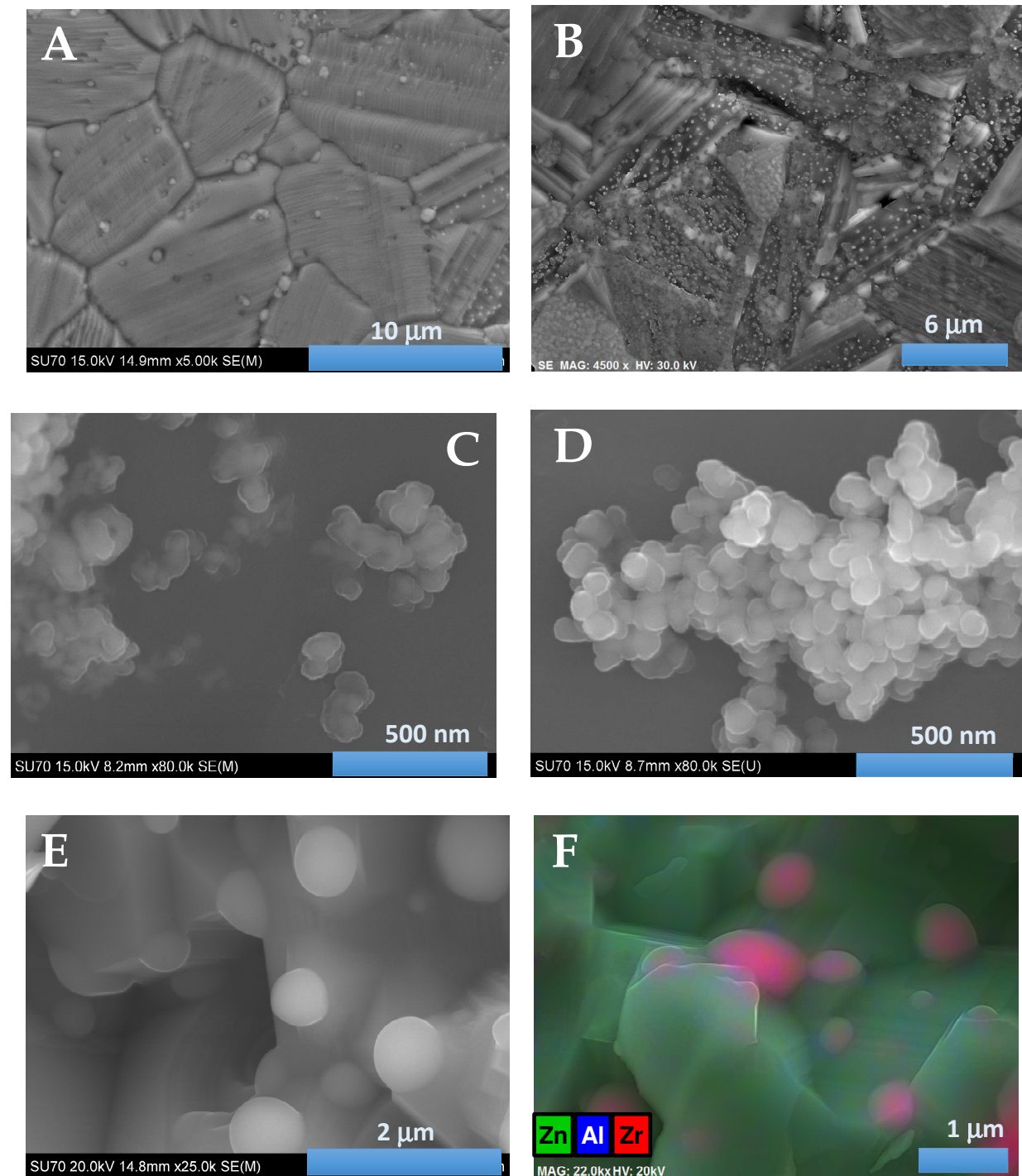


Fig. 2. SEM micrographs of the polished ZN-10 ceramics (A,B), ZrO<sub>2</sub> nanopowder precursors provided by Sigma-Aldrich (C) and Tosoh (D), fractured surface of TZ-20 ceramics (E), and corresponding EDS mapping results for the fractured TZ-20 sample (F).

Thus, one expects that the electrical and thermal transport properties will be rather affected by the presence and morphology of nano- and submicron inclusions and thereby produced effects than by minor differences in the microstructure of the matrix phase. Fig. 2 (E,F) images also confirm a good thermomechanical compatibility between submicron- and nanosized  $\text{ZrO}_2$  inclusions and the  $\text{Zn}_{0.993}\text{Al}_{0.007}\text{O}$  matrix. No cracks were observed at the interfaces between the two phases. The latter is likely realised by the fact that zinc oxide is a relatively soft material<sup>38,39</sup>, thus being capable to accommodate ~20-40% difference in the notably anisotropic thermal expansion of ZnO and monoclinic  $\text{ZrO}_2$ <sup>40-42</sup>.

Further insights into the nanostructural features of the composites are provided by scanning thermal microscopy (SThM), combined with electrostatic force microscopy (EFM). Simultaneous topography and thermal mapping data obtained for the TZ-20 sample are shown in Fig. 3 (A,B). Although the correlation between the topography and thermal signal represent a well-known problem in SThM<sup>43</sup>, a simple comparison of those images indicates that the thermal conductivity contrast provides a reliable information on the relevant contributions of the composite phases. It is clearly seen that the places at the sample possessing negligible topography difference with  $\text{ZrO}_2$  nanoparticles demonstrate a visible SThM contrast (blue marks at Fig. 3 (A,B)). Small (30-100 nm) darker particles correspond to  $\text{ZrO}_2$ , possessing notably lower thermal conductivity<sup>44</sup> as compared to the matrix (lighter area). Secondly, the EFM mapping clearly shows a difference in electrostatic forces over the inclusions and matrix (Fig. 3D) that is not linked to the topography (Fig. 3C), thus, featuring fine  $\text{ZrO}_2$  inclusions. Kelvin probe force microscopy measurements showed a small difference between the work functions of  $\text{Zn}_{0.993}\text{Al}_{0.007}\text{O}$  matrix and  $\text{ZrO}_2$  inclusions (about 10-20 mV). Therefore, the difference in the electrostatic forces is mostly due to a difference of capacitance derivative,

$d^2C/dz^2$ <sup>45</sup>, appeared as result of a several orders conductivity difference between the matrix and inclusions.

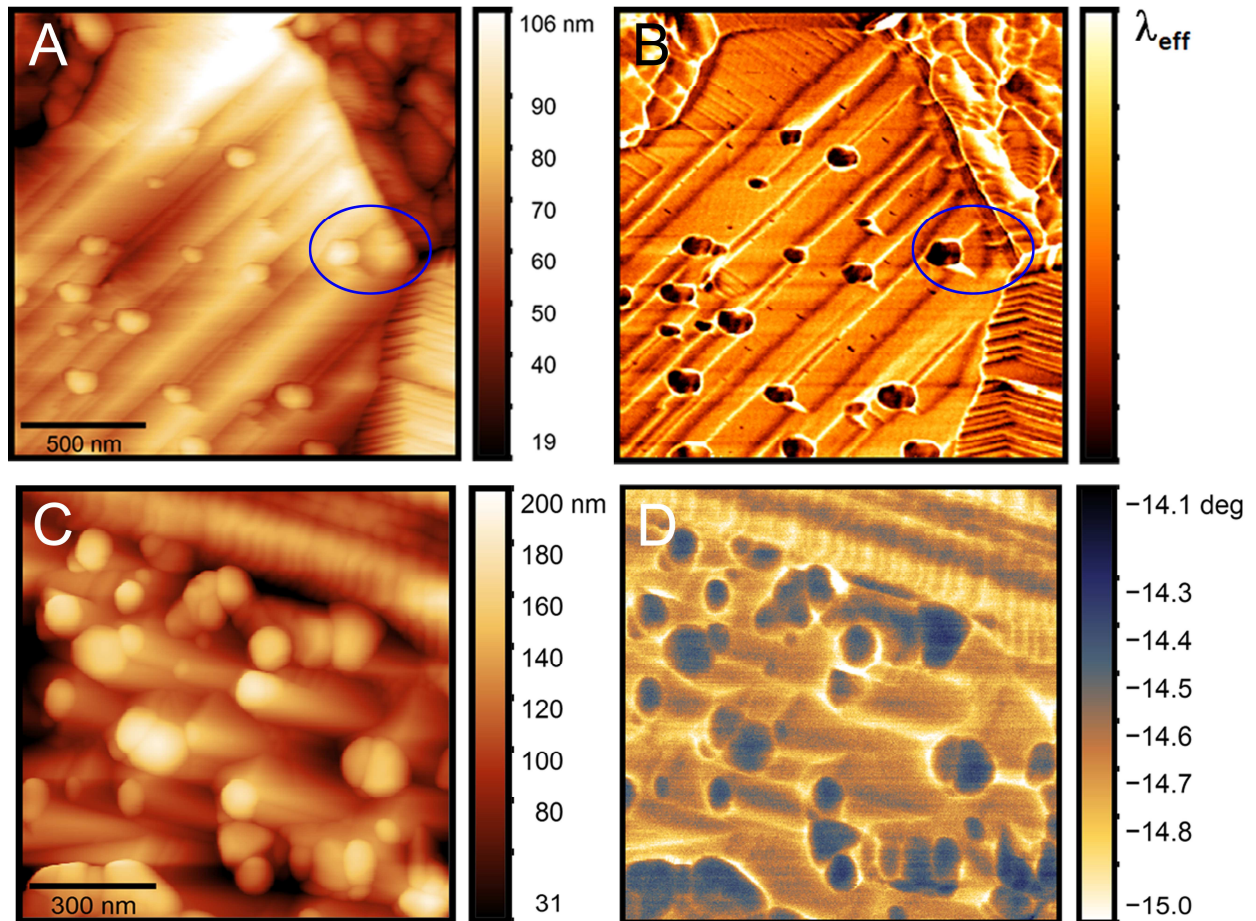


Fig. 3. Topography (A,C) and corresponding thermal conductivity contrast (B) and EFM-phase image (D) for the TZ-20 nanocomposite sample.

The capacitance second derivative difference increases with material conductivity due to better screening of the charges generated by the DC voltage applied to the tip. This leads to the appearance of a negative EFM phase shift. Apparently, the EFM phase is inhomogeneous within the inclusions suggesting that their composition is non-uniform and may be more complex. Yet, the spatial resolution of the used techniques is insufficient to resolve those differences.

The expected tendency for decreasing the thermal conductivity in nanocomposites is clearly visible at temperatures below 700-800 K (Fig. 4A).

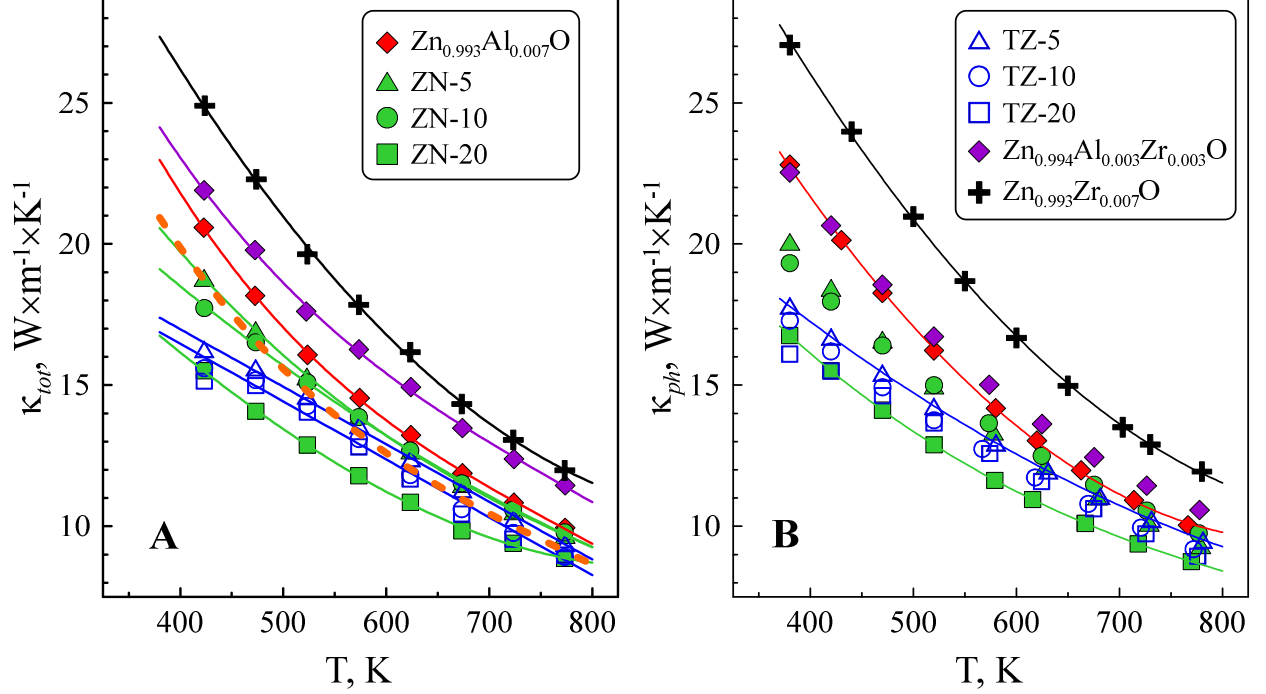


Fig. 4. Total (A) and lattice (B) thermal conductivities of nanocomposites and reference materials. The dashed orange line shows the effective thermal conductivity calculated using a Maxwell approach for composites with spherical inclusions at a ZrO<sub>2</sub> content of 10% wt. The thermal conductivity data for monoclinic ZrO<sub>2</sub> are taken from <sup>44</sup>. The solid lines are for visual guidance only.

This effect is essentially resulting from both the lower thermal conductivity of monoclinic ZrO<sub>2</sub> <sup>44</sup> in comparison to the Zn<sub>0.993</sub>Al<sub>0.007</sub>O matrix and the enhanced phonon scattering at the introduced interfaces. The contribution provided by the difference in the thermal conductivities of the composite phases can be roughly estimated using a Maxwell relation <sup>46</sup>:

$$\frac{\kappa_c}{\kappa_m} = 1 + 3 \frac{\beta - 1}{\beta + 1} \phi \quad (2)$$

where  $\kappa_c$ ,  $\kappa_m$  are the thermal conductivities of the composite and the matrix material,  $\beta$  is the ratio of the thermal conductivities of the spherical particles and the surrounding matrix phase, and  $\phi$  is the volume concentration of the spherical particles. The results shown in Fig. 4A suggest that the nanocomposite concept is particularly effective at temperatures below 500 K, where the phonon mean path is relatively large. Still, a noticeable agglomeration of the ZrO<sub>2</sub> nanoparticles (Fig. 2 A,B) remains the problem that limits an efficient suppressing of the thermal transport and might be responsible for the observed differences in the thermal conductivity behaviour of the ZN and TZ series. At the same time, a comparison of the experimentally observed and calculated thermal conductivity (dashed orange line in Fig. 4A) of the composite containing 10% wt. of ZrO<sub>2</sub> suggests the presence of additional mechanisms behind the reduction of the thermal conductivity in nanocomposites, especially in the case of TZ-series.

The results of combined electrical studies surprisingly revealed an enhanced electronic transport in both ZN- and TZ-series nanocomposites (Fig. 5) at low and moderate ZrO<sub>2</sub> content. The observed difference seems counterintuitive, taking into account that the electrical conductivity of monoclinic ZrO<sub>2</sub> is 5-7 orders of magnitude lower<sup>47</sup> than that of Zn<sub>0.993</sub>Al<sub>0.007</sub>O (Fig. 5A). The observed variations in the Seebeck coefficient are rather moderate (Fig. 5B) and do not consequently follow the usual opposite trend with the electrical conductivity. As an example, the electrical conductivity of the ZN-5 nanocomposite is almost two times higher than for pure Zn<sub>0.993</sub>Al<sub>0.007</sub>O matrix, while corresponding variations in Seebeck coefficient do not exceed 5%. This decoupling between the electrical properties significantly boosts the power factor, as shown in Fig. 5C, reaching up to a ~1.8 times enhancement in the ZN-5 nanocomposite.

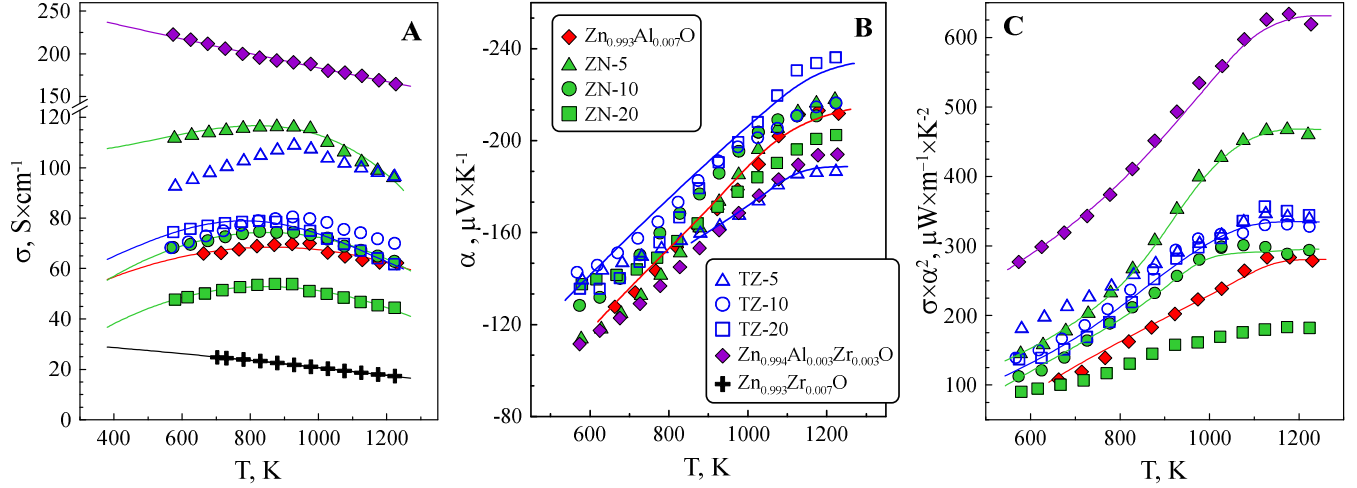


Fig. 5. Electrical properties of nanocomposites and reference ZnO-based materials: electrical conductivity (A), Seebeck coefficient (B) and power factor (C). The solid lines are for visual guidance only.

The obtained results on electrical properties can neither be explained by considering simple mixing rule for composite materials nor by effective medium theory like the Bergman-Fel's theorem<sup>48</sup>. As the electrical conductivity of several nanocomposites significantly exceeds the boundaries defined by the best- ( $\text{Zn}_{0.993}\text{Al}_{0.007}\text{O}$ ) and worst-conducting ( $\text{ZrO}_2$ ) components, the latter suggests the presence of additional mechanisms behind the observed enhancement in the electronic transport. More guidelines can be obtained from the combined SEM/EDS studies at high resolution, as shown in Fig. 6 and 7. The EDS mapping results confirm the presence of fine  $\text{ZrO}_2$  nanoparticles (red), distributed in the matrix, shown as darker background (Fig. 6). The microstructures are quite similar in the case of ZN- (Fig. 6A) and TZ- series (Fig. 6B) nanocomposites. A striking observation is an appearance of additional nanophase, enriched in aluminium, at the interfaces between the zirconia particles and the matrix phase.

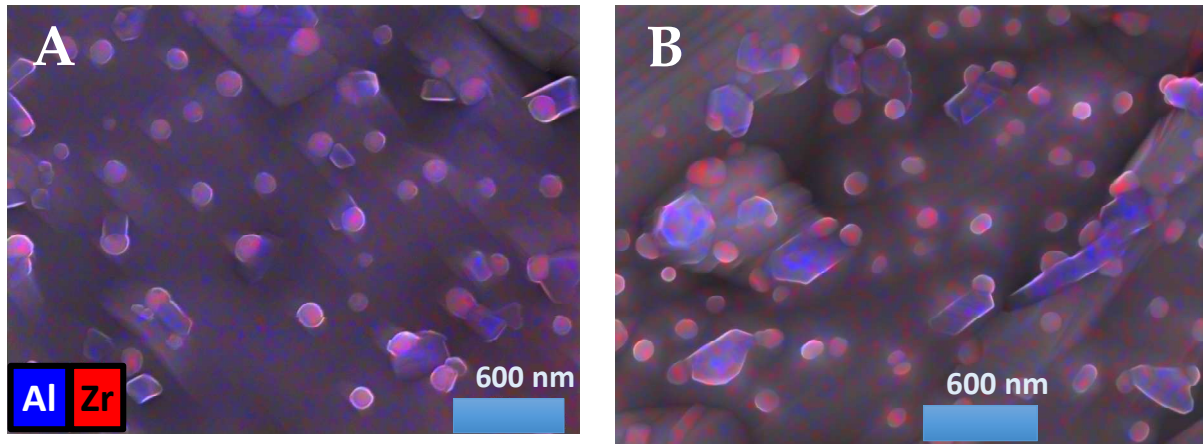


Fig. 6. EDS mapping results showing microstructural evolution in ZN-20 (A) and TZ-20 (B) nanocomposites.

In accordance with the phase diagrams<sup>34,49</sup>, only three phases exist along ZnO-Al<sub>2</sub>O<sub>3</sub> tie-line, namely, wurtzite ZnO, ZnAl<sub>2</sub>O<sub>4</sub> spinel and  $\alpha$ -alumina, whereas no significant interaction between ZrO<sub>2</sub> and Al<sub>2</sub>O<sub>3</sub> is expected under the applied processing conditions<sup>50</sup>. The EDS line scanning profiles (Fig. 7) suggest that the Al-rich nanophase also contains a significant fraction of zinc, as shown by a clear contrast between relative zinc concentrations in ZrO<sub>2</sub> (brighter particles), Al-rich nanophase and Zn<sub>0.993</sub>Al<sub>0.007</sub>O matrix, highlighted by a dashed line. Taking also into account the typical reactions occurring in aluminium-doped zinc oxide<sup>4,21,24</sup>, one can identify the new nanophase as ZnAl<sub>2</sub>O<sub>4</sub> spinel. It is noteworthy that this phase was not detected by the XRD studies (Fig. 1), most likely due to its relatively low content set by the nominal Zn<sub>0.993</sub>Al<sub>0.007</sub>O matrix composition. Similar inconsistency between the XRD results and microstructural observations was revealed in the work<sup>21</sup>; the phase identification by XRD is also complicated by the fact that the main ZnAl<sub>2</sub>O<sub>4</sub> peak ( $\sim 36.7$ - $36.8^\circ$ ) is partially overlapped with one of those corresponding to the wurtzite phase.

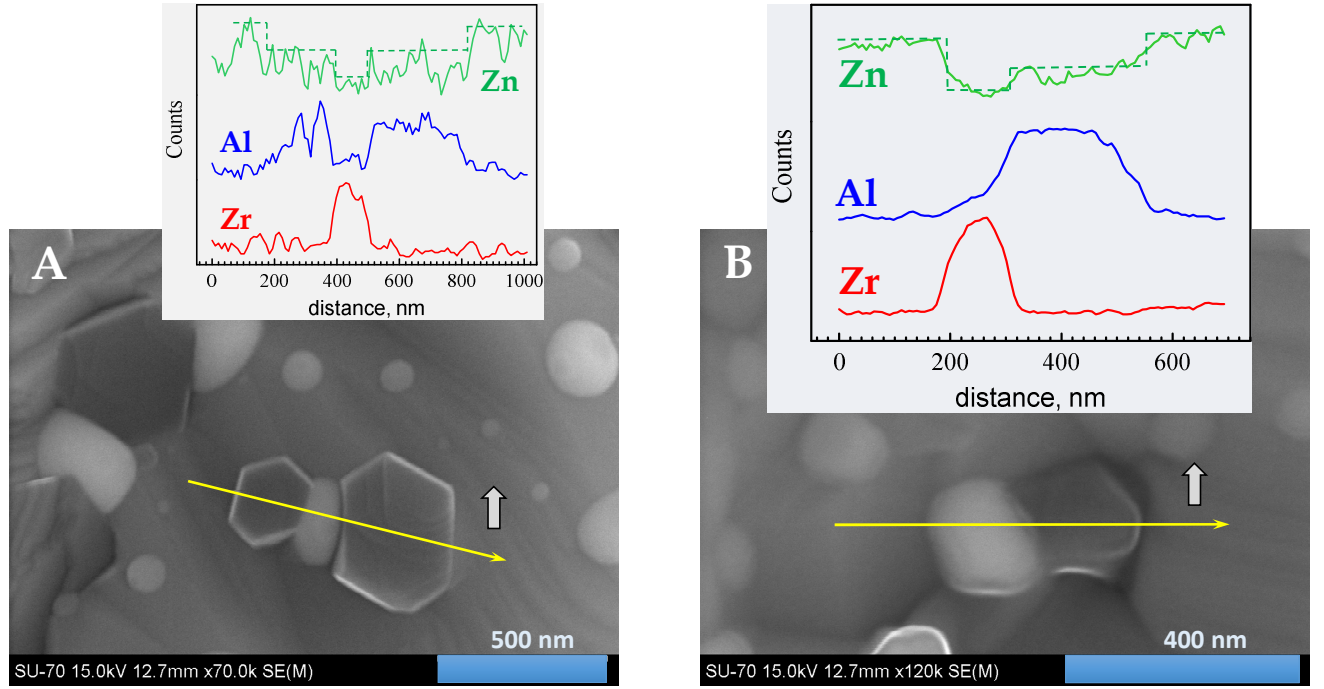
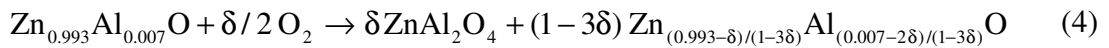
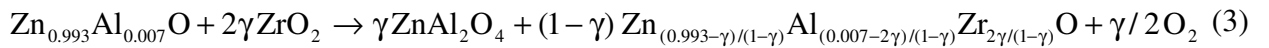


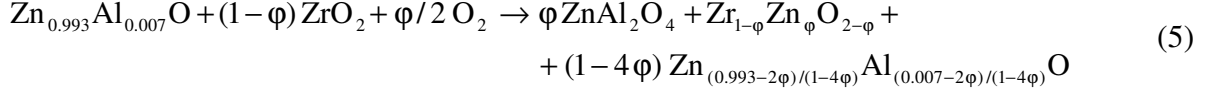
Fig. 7. EDS line scanning profiles showing the cation distribution in nanophases present in ZN-20 (A) and TZ-20 (B) nanocomposites. The dashed line highlights the evolution of zinc content in the matrix and nanoparticles.

The spinel phase is being likely formed by one of the following reactions or their combination:



where  $\gamma$  and  $\delta$  are the fractions of reacted  $\text{ZrO}_2$  and decomposed matrix composition, respectively. The reaction (Eq. 3) involves a partial replacement of  $\text{Al}^{3+}$  by  $\text{Zr}^{4+}$  cations as a driving force for the spinel formation, while the scheme (Eq. 4) represents a known decomposition reaction, often responsible for affecting the thermal transport and electronic conduction in ZnO-based thermoelectrics<sup>3,21,24,25,35</sup>. One may also account for the partial

substitution of zirconium in  $ZrO_2$  by zinc <sup>51</sup>, accompanied by the segregation of  $ZnAl_2O_4$  to compensate for the cation stoichiometry change in the matrix phase:



where  $\varphi$  represents the fraction of reacted zirconia.

Typical effects imposed by the formation of  $ZnAl_2O_4$  nanophase include more efficient phonon scattering by numerous additional interfaces and partial blocking of the electronic transport. The reactions Eq. 3 and Eq. 5 yield insulating spinel, while also resulting in a decrease of the donor-doping level and, correspondingly, the concentration of the charge carriers. Any noticeable contribution provided by the onset of ionic conduction in zirconia due to substitution by zinc can be neglected, based both on typical conductivity values fairly below 0.1 S/cm <sup>52</sup> in such materials under discussed conditions and absence of percolation in the dispersed phase. Thus, the reactions (Eqs. 4-5) are not expected to promote higher electrical performance in nanocomposites (Fig. 5A). The electrical conductivity data for the reference samples with a nominal composition of  $Zn_{0.994}Al_{0.003}Zr_{0.003}O$  and  $Zn_{0.993}Zr_{0.007}O$  (Fig. 5A), however, suggests that the matrix interaction with the dispersed  $ZrO_2$  phase yielding mixed doping (Eq. 3) may be responsible for the observed conductivity increase. It should be noticed that a similar improvement of the electrical conductivity in the mixed-doped materials was previously observed for Al- and Ni- co-doped  $ZnO$  <sup>23,53,54</sup>. This behaviour was attributed to the favourable microstructural evolution, promoting the charge transport <sup>23</sup>, and to an increase in the charge carrier concentration <sup>53,54</sup>. In particular, the presence of nickel cations was found to enhance the aluminium solubility through various mutual effects including lattice expansion due to nickel incorporation into the interstitial positions, which, in turn, favours aluminium substitution for

zinc and generation of extra charge carriers<sup>53</sup>. Similar effects in Al- and Zr- co-doped ZnO may lead to the significant boosting of the electrical conductivity observed for  $\text{Zn}_{0.994}\text{Al}_{0.003}\text{Zr}_{0.003}\text{O}$  as compared to  $\text{Zn}_{0.993}\text{Al}_{0.007}\text{O}$  and  $\text{Zn}_{0.993}\text{Zr}_{0.007}\text{O}$  (Fig. 5A). Still, the solubility of zirconium in the ZnO lattice is very limited, as confirmed by the XRD results (Fig. 1) and the relatively low electrical conductivity of  $\text{Zn}_{0.993}\text{Zr}_{0.007}\text{O}$ . The lattice thermal conductivity of  $\text{Zn}_{0.993}\text{Zr}_{0.007}\text{O}$  is also the highest among all studied materials (Fig. 4B), which might be considered as a fingerprint of the lowest concentration of the point defects, promoted by doping. A large difference in the electronegativity between  $\text{Zr}_{\text{Zn}}^{\bullet\bullet}$  point defects and host lattice cations may also facilitate scattering of the charge carriers and cause a significant reduction in the mobility, thus decreasing the electrical conductivity<sup>55</sup>.

The described behaviour actually suggests a concept of self-forming nanocomposite as a tool to tailor the thermoelectric performance of ZnO-based materials, where, by introducing a nano-dispersed phase with limited reactivity and processing at high temperatures, the controlled interaction with the matrix is promoted, resulting in an appearance of an additional nanophase. This process is well-illustrated by EDS line scanning profile (Fig. 7), showing the formation of a  $\text{ZnAl}_2\text{O}_4$  spinel nanophase next to the  $\text{ZrO}_2$  nanoparticles. The interactions boost the electrical transport through the matrix phase due to synergistic co-doping effects, whose mechanisms are yet not well understood, while also contributing to the phonon scattering and consequently decreasing the lattice thermal conductivity as compared to the reference compositions (Fig. 4B). As a result, at 920-1200 K the dimensionless figure-of-merit  $ZT$  of the ZN-5 nanocomposite is almost twice of the pure matrix composition (Fig. 8).

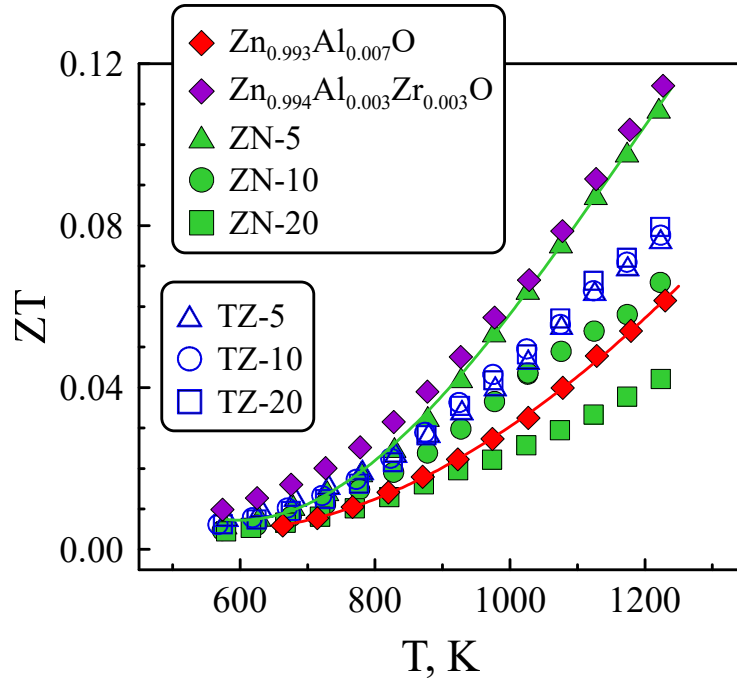


Fig. 8. Temperature dependence of the ZT values for the pure matrix-phase and nanocomposite samples. The solid lines are for visual guidance only.

It is noteworthy that a certain enhancement was attained for all nanocomposite series, except the ZN-20 formulation. The performance of the TZ-series composites is quite similar to each other, thus showing a distinctly different behaviour compared to ZN series. Following the results shown in the Figs. 4A and 5C, both power factor and thermal conductivity of TZ-5, TZ-10 and TZ-20 do not vary significantly with  $ZrO_2$  content, in opposite to the clear changes observed in ZN series. This behaviour might be related to the differences in chemical reactivity of Sigma-Aldrich and Tosoh zirconia powders, and, possibly, to their inherent tolerance to agglomeration; this requires additional studies to be addressed. In particular, the extent of reaction between zirconia powder and the matrix is expected to affect both modification of the host matrix and exsolution of the nanophases. Thus, on altering  $ZrO_2$  concentration various mutual effects might be observed, including self-compensation of the increase in electrical conductivity on mixed-doping by concomitant decrease of the Seebeck coefficient in TZ series (Fig. 5), and a balance between the thermal conductivity decrease due to exsolution of the nanophases and presence of

ZrO<sub>2</sub>, and possible increase in thermal transport in mixed-doped compositions, as observed for Zn<sub>0.994</sub>Al<sub>0.003</sub>Zr<sub>0.003</sub>O (Fig. 4). Still, all TZ-nanocomposites show favourable decoupling of the electrical and thermal transport properties towards enhanced thermoelectric performance, as compared to the pure matrix composition.

One should notice that a ZT increase in the nanocomposites is mainly originated by boosting the electrical contribution, while the thermal conductivity still remains excessively high. The estimated phonon mean path at room temperature in ZnO-based materials corresponds to ~30 nm<sup>56</sup>, requesting a similar particle size to provide an efficient phonon scattering. It might be anticipated that a corresponding decrease in the spinel particle size is achievable through further optimization of the processing conditions (e.g.,<sup>21,22,24</sup>). This possibility for optimization is also supported by the observed lower thermal conductivity of TZ-10 nanocomposite at T < 500 K, as compared to that calculated using Maxwell relation (Eq. 2, Fig. 4A), while the corresponding difference with ZN-10 composition was rather minor.

Another important issue is the long-term stability of ZnO-based thermoelectrics under elevated temperatures, known as one of the major concerns limiting the potential applications<sup>13,14</sup>. The effect of ageing in these materials is mostly linked to the deterioration of the electrical properties rather than the thermal conductivity, which may be even suppressed by the exsolution of the dopant cations from wurtzite lattice at the nanoscale level. The results of stability tests, performed for electrical conductivity and Seebeck coefficient are presented in Fig. 9.

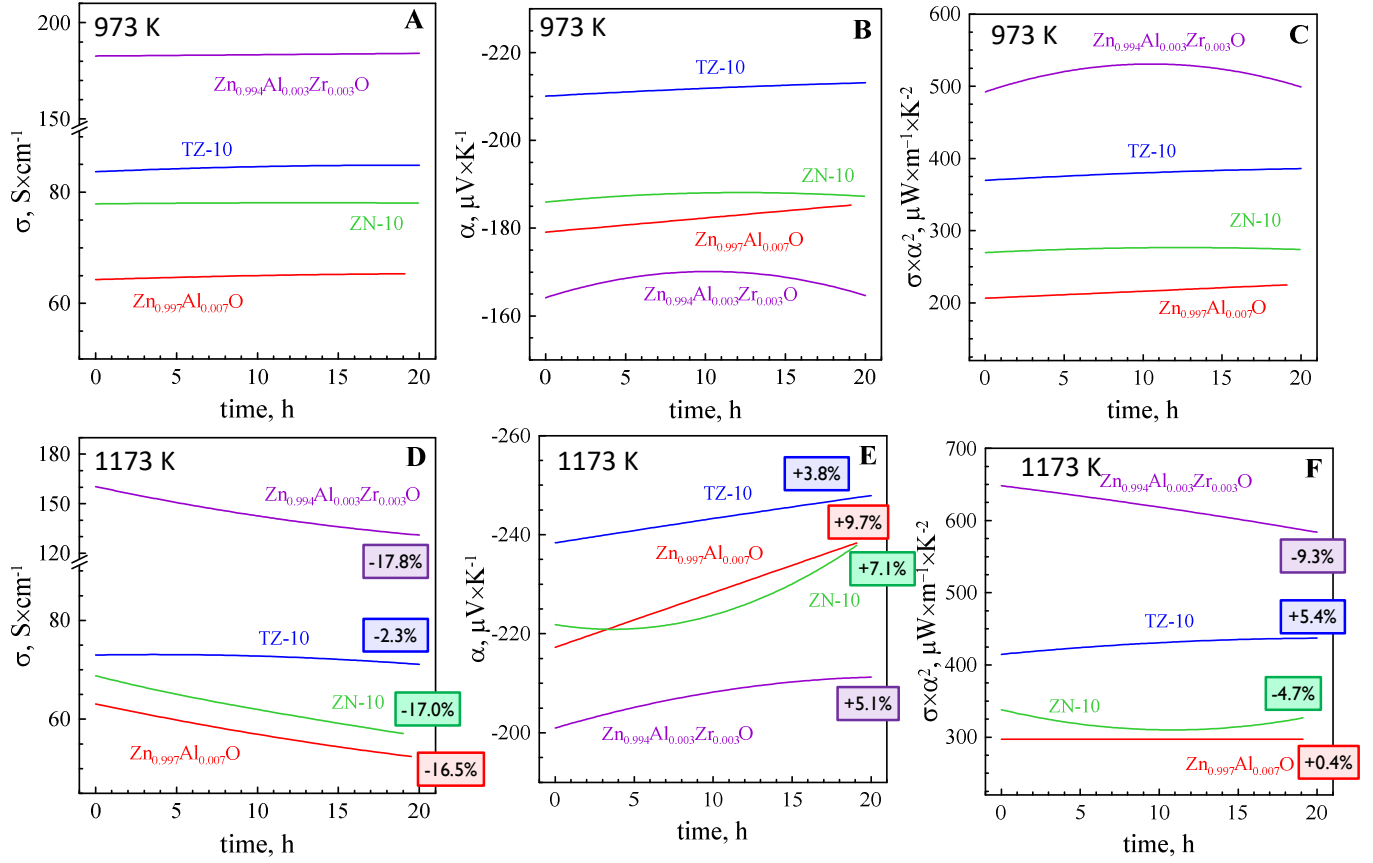


Fig. 9. Time dependence of the electrical conductivity (A,D), Seebeck coefficient (B,E) and power factor (C,F) at 973 K (A, B, C) and 1173 K (D, E, F) for the matrix  $\text{Zn}_{0.993}\text{Al}_{0.007}\text{O}$  and reference  $\text{Zn}_{0.994}\text{Al}_{0.003}\text{Zr}_{0.003}\text{O}$  compositions, and two representative ZN-10 and TZ-10 nanocomposites. The extent of evolution of the thermoelectric properties at 1173 K is shown in % for each composition.

The evolution of electrical properties was monitored during 20 h in air at 973 and 1173 K. Essentially stable performance was observed at 973 K (Fig. 9A-C), with some indications of the presence of relaxation processes affecting the Seebeck coefficient, mostly pronounced for  $\text{Zn}_{0.994}\text{Al}_{0.003}\text{Zr}_{0.003}\text{O}$  composition. Thus, this temperature may be still acceptable for the hot side of thermoelectric modules based on the studied compositions. Higher temperatures promote the simultaneous reduction in the electrical conductivity and an increase in Seebeck coefficient, a fingerprint of diminution of the charge carrier concentration, except for TZ-10 nanocomposite.

Corresponding decrease/increase in %, indicated in Fig. 9D-F, allow to compare the evolution in performance for various compositions. Although the relative decrease in electrical conductivity observed for the mixed  $\text{Zn}_{0.994}\text{Al}_{0.003}\text{Zr}_{0.003}\text{O}$  sample is comparable to that of the  $\text{Zn}_{0.993}\text{Al}_{0.007}\text{O}$  matrix and ZN-10 nanocomposite, it is accompanied with only a moderate increase in the Seebeck coefficient. On the contrary, an increase in Seebeck coefficient observed for the ZN-10 partially compensates the conductivity decrease to maintain a relatively high power factor. Whatever is the exact mechanism of such behaviour for both ZN- and TZ-series, the results suggest that more stable electrical performance may be achieved in such nanocomposites. In particular, although the overall performance of mixed-doped  $\text{Zn}_{0.994}\text{Al}_{0.003}\text{Zr}_{0.003}\text{O}$  is comparable to the ZN-5, the composite formulations may be more advantageous for high-temperature applications when considering the degradation issues. One may anticipate that such stabilization behaviour can be related to the buffer effects at the interfaces between  $\text{ZrO}_2$  and matrix phase, which may precondition the donor-doping level at the grain boundaries and restrict continuous exsolution of the dopant cations. Still, this hypothesis requires additional electrical and microstructural studies, supported by monitoring of the structural evolution with time.

Although the highest observed performance is still lower than attained for some ZnO-based thermoelectrics (e.g., those sintered from nanopowders using SPS technique<sup>22,24,25</sup>), the results provide a clear insight on how electrical and thermal transport can be simultaneously improved in these materials. Thus, the concept of a self-forming composite with controlled interactions between the components may open new pathways for decoupling the electrical and thermal transport parameters in oxide thermoelectrics. Namely, the possibilities for moderate improvement of the power factor in composites, predicted by effective medium theories, can be further enhanced by the interplay between exsolution of nanophases and modification of the host lattice, which proceed in a controllable manner and impart low thermal conductivity along with better electrical performance. At the same time, the donor-doping level at the grain boundaries is

to a certain extent preconditioned by the presence of a dispersed phase, inasmuch as the constituting cations are slightly soluble in the matrix host lattice and the thermal history of the sample. Hence, foreseen flexibility constitutes another advantage of the proposed approach, with clear prospects for implementation in other thermoelectric oxide systems.

#### **4. Conclusions**

ZnO-based nanocomposites were prepared by ultrasonic dispersion of ZrO<sub>2</sub> nanoparticles in Zn<sub>0.993</sub>Al<sub>0.007</sub>O powder, followed by sintering to obtain dense ceramic samples. Combined electrical and thermal conductivity studies have demonstrated that the addition of ZrO<sub>2</sub> nanoparticles results in suppressing the thermal transport due to both a lower intrinsic thermal conductivity of monoclinic zirconia and introducing new phonon scattering interfaces, while the power factor was up to ~1.8 times enhanced at high temperatures. The observed behaviour was attributed to the formation of an additional spinel ZnAl<sub>2</sub>O<sub>4</sub> nanophase next to the dispersed ZrO<sub>2</sub> particles, promoted by the interaction of the initial composite components, and corresponding changes in the chemical composition of the Zn<sub>0.993</sub>Al<sub>0.007</sub>O matrix. The observed enhancement of the thermoelectric performance in nanocomposites was mainly provided by boosting the electrical contribution, while the thermal conductivity still remains excessively high. Comparative isothermal studies of the electrical performance in nanocomposites and reference materials revealed faster degradation of the power factor in mixed-doped composition, indicating that the composite formulations may be more advantageous for high-temperature applications provided by the stability issues. The concept of a self-forming composite with controlled interaction between the components may open new pathways for an independent tuning of the electrical and thermal transport properties in oxide thermoelectrics.

### **Acknowledgements**

This work was supported by the FCT, including individual grant IF/00302/2012, project CICECO-Aveiro Institute of Materials (ref. UID/CTM/50011/2013), project of bilateral cooperation between FCT and DAAD (Germany) and the projects POCI-01-0145-FEDER-031875 and POCI-01-0145-FEDER-032117, financed by COMPETE 2020 Program and National Funds through the FCT/MEC and when applicable co-financed by FEDER under the PT2020 Partnership Agreement. The authors are thankful to Artur Sarabando (University of Aveiro) and to Dr. P. Thiel (Empa) for their technical and experimental support.

## References

- 1 H. Morkoç and Ü. Özgür, *Zinc Oxide: Fundamentals, Materials and Device Technology*, Wiley-VCH Verlag GmbH & Co. KGaA, Weinheim, Germany, Germany, 2009.
- 2 Ü. Özgür, Y. I. Alivov, C. Liu, A. Teke, M. A. Reshchikov, S. Doğan, V. Avrutin, S. J. Cho and H. Morkoç, *J. Appl. Phys.*, 2005, **98**, 1–103.
- 3 T. Tsubota, M. Ohtaki, K. Eguchi and H. Arai, *J. Mater. Chem.*, 1997, **7**, 85–90.
- 4 M. Ohtaki, T. Tsubota, K. Eguchi and H. Arai, *J. Appl. Phys.*, 1996, **79**, 1816–1818.
- 5 D. M. Rowe, *Modules, Systems, and Applications in Thermoelectrics*, CRC Press, 2012.
- 6 A. Date, A. Date, C. Dixon and A. Akbarzadeh, *Renew. Sustain. Energy Rev.*, 2014, **33**, 371–381.
- 7 M. Backhaus-Ricoult, J. Rustad, L. Moore, C. Smith and J. Brown, *Appl. Phys. A Mater. Sci. Process.*, 2014, **116**, 433–470.
- 8 K. Koumoto, R. Funahashi, E. Guilmeau, Y. Miyazaki, A. Weidenkaff, Y. Wang and C. Wan, *J. Am. Ceram. Soc.*, 2013, **96**, 1–23.
- 9 J. D. Baran, D. Kepaptsoglou, M. Molinari, N. Kulwongwit, F. Azough, R. Freer, Q. M. Ramasse and S. C. Parker, *Chem. Mater.*, 2016, **28**, 7470–7478.
- 10 J. F. Li, W. S. Liu, L. D. Zhao and M. Zhou, *NPG Asia Mater.*, 2010, **2**, 152.
- 11 A. A. V. Kovalevsky, M. H. M. H. Aguirre, S. Populoh, S. G. S. G. Patrício, N. M. N. M. Ferreira, S. M. S. M. Mikhalev, D. P. Fagg, A. Weidenkaff and J. Frade, *J. Mater. Chem. A*, 2017, **5**.
- 12 J. He, S. Hao, Y. Xia, S. S. Naghavi, V. Ozoliņš and C. Wolverton, *Chem. Mater.*, 2017, **29**, 2529–2534.
- 13 L. Han, D. V. Christensen, A. Bhowmik, S. B. Simonsen, L. T. Hung, E. Abdellahi, Y. Z. Chen, N. V. Nong, S. Linderoth and N. Pryds, *J. Mater. Chem. A*, 2016, **4**, 12221–12231.
- 14 N. Vogel-Schäuble, R. Dujardin, A. Weidenkaff and M. H. Aguirre, *J. Electron. Mater.*, 2012, **41**, 1606–1614.
- 15 A. J. Minnich, M. S. Dresselhaus, Z. F. Ren and G. Chen, *Energy Environ. Sci.*, 2009, **2**, 466.
- 16 K. Biswas, J. He, I. D. Blum, C.-I. Wu, T. P. Hogan, D. N. Seidman, V. P. Dravid and M. G. Kanatzidis, *Nature*, 2012, **489**, 414–8.
- 17 M. Samanta, S. Roychowdhury, J. Ghatak, S. Perumal and K. Biswas, *Chem. - A Eur. J.*, 2017, **23**, 7438–7443.
- 18 Z. L. Wang, *Mater. Today*, 2004, **7**, 26–33.
- 19 Zheng Wei Pan, Zu Rong Dai and Zhong Lin Wang, *Science (80-. )*, 2001, **291**, 1947–1949.

- 20 Y. Kinemuchi, H. Nakano, M. Mikami, K. Kobayashi, K. Watari and Y. Hotta, *J. Appl. Phys.*, 2010, **108**, 053721.
- 21 P. Jood, R. J. Mehta, Y. Zhang, G. Peleckis, X. Wang, R. W. Siegel, T. Borca-Tasciuc, S. X. Dou and G. Ramanath, *Nano Lett.*, 2011, **11**, 4337–4342.
- 22 L. Han, N. Van Nong, W. Zhang, L. T. Hung, T. Holgate, K. Tashiro, M. Ohtaki, N. Pryds and S. Linderoth, *R. Soc. Chem. Adv.*, 2014, **4**, 12353.
- 23 K. H. Kim, S. H. Shim, K. B. Shim, K. Niihara and J. Hojo, *J. Am. Ceram. Soc.*, 2005, **88**, 628–632.
- 24 D. Gautam, M. Engenhorst, C. Schilling, G. Schierning, R. Schmechel and M. Winterer, *J. Mater. Chem. A*, 2015, **3**, 189–197.
- 25 D.-B. Zhang, H.-Z. Li, B.-P. Zhang, D. Liang and M. Xia, *RSC Adv.*, 2017, **7**, 10855–10864.
- 26 J. Eichler, U. Eisele and J. Rödel, *J. Am. Ceram. Soc.*, 2004, **87**, 1401–1403.
- 27 A. V. V. Kovalevsky, A. A. A. Yaremchenko, S. Populoh, A. Weidenkaff and J. R. R. Frade, *J. Appl. Phys.*, 2013, **113**, 053704.
- 28 L. J. Brillson and Y. Lu, *J. Appl. Phys.*, 2011, **109**, 121301.
- 29 L. Zhang, T. Tosho, N. Okinaka and T. Akiyama, *Mater. Trans.*, 2008, **49**, 2868–2874.
- 30 J. Rodríguez-Carvajal, *Phys. B Condens. Matter*, 1993, **192**, 55–69.
- 31 H. G. Scott, *J. Mater. Sci.*, 1975, **10**, 1527–1535.
- 32 C. Schilling, M. Zähres, C. Mayer and M. Winterer, *J. Nanoparticle Res.*, 2014, **16**, 2506.
- 33 T. Tian, L. Cheng, L. Zheng, J. Xing, H. Gu, S. Bernik, H. Zeng, W. Ruan, K. Zhao and G. Li, *Acta Mater.*, 2016, **119**, 136–144.
- 34 M. Kim, S. Lai and R. M. Laine, *J. Am. Ceram. Soc.*, 2011, **94**, 3308–3318.
- 35 K. F. Cai, E. Müller, C. Drašar and A. Mrotzek, *Mater. Sci. Eng. B Solid-State Mater. Adv. Technol.*, 2003, **104**, 45–48.
- 36 F. Giovannelli, A. Ngo Ndimba, P. Diaz-Chao, M. Motelica-Heino, P. I. Raynal, C. Autret and F. Delorme, *Powder Technol.*, 2014, **262**, 203–208.
- 37 E. Guilmeau, P. Díaz-Chao, O. I. Lebedev, A. Rečnik, M. C. Schäfer, F. Delorme, F. Giovannelli, M. Košir and S. Bernik, *Inorg. Chem.*, 2017, **56**, 480–487.
- 38 S. O. Kucheyev, J. E. Bradby, J. S. Williams, C. Jagadish and M. V. Swain, *Appl. Phys. Lett.*, 2002, **80**, 956–958.
- 39 A. Hernández Battez, R. González, J. L. Viesca, J. E. Fernández, J. M. Díaz Fernández, A. Machado, R.

- Chou and J. Riba, *Wear*, 2008, **265**, 422–428.
- 40 H. Ibach, *Phys. Status Solidi*, 1969, **33**, 257–265.
- 41 J. W. Adams, H. H. Nakamura, R. P. Ingel and R. W. Rice, *J. Am. Ceram. Soc.*, 1985, **68**, C??228-C??231.
- 42 R. N. Patil and E. C. Subbarao, *J. Appl. Crystallogr.*, 1969, **2**, 281–288.
- 43 M. J. Pereira, J. S. Amaral, N. J. O. Silva and V. S. Amaral, *Microsc. Microanal.*, 2016, **22**, 1270–1280.
- 44 R. K. Williams, J. B. Bates, R. S. Graves, D. L. McElroy and F. J. Weaver, *Int. J. Thermophys.*, 1988, **9**, 587–598.
- 45 C. Staii, A. T. Johnson and N. J. Pinto, *Nano Lett.*, 2004, **4**, 859–862.
- 46 A. S. Sangani and C. Yao, *J. Appl. Phys.*, 1988, **63**, 1334–1341.
- 47 O. H. Kwon, C. Jang, J. Lee, H. Y. Jeong, Y. il Kwon, J. H. Joo and H. Kim, *Ceram. Int.*, 2017, **43**, 8236–8245.
- 48 D. J. Bergman and L. G. Fel, *J. Appl. Phys.*, 1999, **85**, 8205–8216.
- 49 E. M. Levin, *Phase Diagrams for Ceramists*, American Ceramic Society, Westerville, Ohio, 1964.
- 50 D. A. Jerebtsov, G. G. Mikhailov and S. V. Sverdina, *Ceram. Int.*, 2000, **26**, 821–823.
- 51 G. Štefanić, S. Musić and M. Ivanda, *J. Mol. Struct.*, 2009, **924–926**, 225–234.
- 52 C. Ahamer, A. K. Opitz, G. M. Rupp and J. Fleig, *J. Electrochem. Soc.*, 2017, **164**, F790–F803.
- 53 D. B. Zhang, B. P. Zhang, D. S. Ye, Y. C. Liu and S. Li, *J. Alloys Compd.*, 2016, **656**, 784–792.
- 54 H. Yamaguchi, Y. Chonan, M. Oda, T. Komiyama, T. Aoyama and S. Sugiyama, *J. Electron. Mater.*, 2011, **40**, 723–727.
- 55 T. Tsubota, M. Ohtaki, K. Eguchi and H. Arai, *J. Mater. Chem.*, 1998, **8**, 409–412.
- 56 S. Leblanc, S. Phadke, T. Kodama, A. Salleo and K. E. Goodson, *Appl. Phys. Lett.*, 2012, **100**, 163105.